Study on solids translational and rotational motions in rotating cans

Yang, Z; Fan, H.; Parker, David; Fryer, Peter; Bakalis, S.; Fan, X.

DOI:
10.1016/j.lwt.2013.12.047

Document Version
Publisher's PDF, also known as Version of record

Citation for published version (Harvard):
Yang, Z, Fan, H, Parker, D, Fryer, P, Bakalis, S & Fan, X 2014, 'Study on solids translational and rotational motions in rotating cans', *LWT - Food Science and Technology*, vol. 57, no. 1, pp. 383-392. https://doi.org/10.1016/j.lwt.2013.12.047

LWT - Food Science and Technology 57 (2014) 383–392

Contents lists available at ScienceDirect

LWT - Food Science and Technology

journal homepage: www.elsevier.com/locate/lwt

Study on solids translational and rotational motions in rotating cans

Z. Yang [a,b,*], H. Fan [c], D.J. Parker [a], P.J. Fryer [b], S. Bakalis [b], X. Fan [d]

[a] School of Physics and Astronomy, University of Birmingham, Birmingham B15 2TT, UK
[b] School of Chemical Engineering, University of Birmingham, Birmingham B15 2TT, UK
[c] School of Medicine, University of Birmingham, Birmingham B15 2TT, UK
[d] School of Engineering, The University of Edinburgh, Edinburgh EH9 3JL, UK

ARTICLE INFO

Article history:
Received 17 May 2012
Received in revised form
4 October 2013
Accepted 30 December 2013

Keywords:
Multiphase flow
Solids rotation
Rotation reconstruction
Location algorithm
Multiple-Positron Emission Particle Tracking

ABSTRACT

Study on translational and rotational motion of solids is important in a wide range of engineering processes. However, rotational motion of solid particles in an opaque system has not been given much attention due to the lack of appropriate measurement methods. This paper presents a new technique, Multiple-Positron Emission Particle Tracking (Multiple-PEPT), to track both rotational and translational motions of a solid simultaneously. The sample study presented here is to track the rotation and translation of a cubed potato in a food can for optimising the canned food process. The results have demonstrated that the rotational and transitional motion of the cubed potato can be simultaneously tracked through mounting three small (200 microns) radioactive tracers on the cube corners. The rotation and translation of the cube can be reconstructed based on the trajectories of the three tracers. The translational and rotational motions of the potato particle are related to each other, and both the motions are greatly dependent on the solids fraction, the liquid viscosity and the density difference between the solid and liquid; but follow specific patterns.

1. Introduction

Solids motion can be classified into translational and rotational motions, and both of them play an important role in heat and mass transfer in a wide range of engineering processes. For example, a number of food processing problems involve the transport and thermal processing of solid–liquid mixtures that are of high solids fraction (often >40%) and with carrier fluids that are viscous and non-Newtonian (Barigou, Mankad, & Fryer, 1998; Lareo, Branch, & Fryer, 1997; Lareo, Nedderman, & Fryer, 1997). The heat transfer coefficient between solid and liquid is critical in determining process times and overall product characteristics, and is greatly dependent on both rotational and translational behaviours of the solid. The translational motion controls the residence time of solids in different position of the process (Fairhurs, Barigou, Fryer, Pain, & Parker, 2001), while the rotational motion is significant in defining the interphase heat transfer coefficients which may control the particle heating and cooling rates (Mankad, Branch, & Fryer, 1995; Mankad & Fryer, 1997; Mankad, Nixon, & Fryer, 1997).

A number of studies have focused on fluid dynamics of food flows and heat transfer in order to optimize thermal processes, and to minimize the heat applied to ensure commercial sterility or pasteurization without unacceptable quality loss (Kızıltaş, Erdoğdu, & Palazoğlu, 2010; Legrand, Berthou, & Fillaudeau, 2007), such as quantifying solid rotation by using high-speed photography to capture the marked solids (such as Kale, Ramezan, & Anderson, 1989; Lee & Hsu, 1996; Tsuji, Morkawa, & Mizumo, 1985; White, 1982; White & Schulz, 1977). However, optical tracking techniques are limited to transparent systems and suffer a low resolution due to refraction of light. A significant amount of food is processed after packing into cans or pouches, and the solid and liquid motions cannot be tracked through optical technique. A number of models have been developed for such systems, such as Chen and Ramaswamy (2002), García, Balsa-Canto, Alonso, Banga (2006), Miri et al. (2008), Abdul Ghani and Farid (2006), Jun and Sastry (2007), Kannan and Sandaka (2008).

Positron Emission Particle Tracking (PEPT) was developed at the University of Birmingham for tracking a single particle accurately and non-invasively (Bakalis, Cox, Russell, Parker, & Fryer, 2006; Cox et al., 2003; Parker, Broadbent, Fowles, Hawkesworth, & McNeil, 1993; Yang, Fan, Bakalis, Parker, & Fryer, 2008a). The significant advantage of the method is that PEPT can track particles accurately through 20–30 mm of metal. The equipment used thus need not be

* Corresponding author. School of Physics and Astronomy, University of Birmingham, Birmingham B15 2TT, UK. Tel.: +44 121 414 4705; fax: +44 121 414 4719.
E-mail address: Yangzw@bham.ac.uk (Z. Yang).

0023-6438/$ – see front matter © 2014 Elsevier Ltd. All rights reserved.
http://dx.doi.org/10.1016/j.lwt.2013.12.047

transparent as with particle imagery velocimetry (PIV) (Duursma, Glass, Rix, & Yorquez-Ramirez, 2001) or be metal free as with magnetic resonance imaging (MRI) experiments (Reyes, Lafi, & Saloner, 1998). The technique has been recently further improved to track three particles simultaneously (Yang, Parker, Fryer, Bakalis, & Fan, 2006). This makes it possible to track both translational and rotational motions of a particle simultaneously. Yang, Fan, Bakalis, Parker, and Fryer (2008b) presented the algorithm, and have demonstrated the use of the method for one simple case.

In this study the solids behaviours in a rotating can system are investigated systematically using our newly developed technique called Multiple-PEPT. The translational motion gives the solids velocity profile, whilst from the rotational motion the distribution of rotational speed is constructed. The aim of the work is to demonstrate the method and to give data which can be incorporated into future models of food flows.

2. Experimental methods and materials

Experimental methods consist of Multiple-PEPT and reconstruction of the translational and rotational motions by three tracked tracers, described as follows.

2.1. Multiple-PEPT technique

The technique involves a positron camera at the University of Birmingham, radioactively labelled tracers (Fan, Parker, & Smith, 2006a, 2006b), and a location algorithm used for calculating the tracer location and speed. The camera consists of two position-sensitive detectors to detect pairs of 511 keV γ-rays as shown in Fig. 1. Each detector has an active area of 500 × 400 mm^2. The tracer particles are 200-micron resin beads which are labelled with radionuclide ^{18}F. Three of the labelled resins beads were mounted to different corners of a potato cube. ^{18}F has a short half-life of 109 min. It will decay to oxygen next morning. The nuclear dose used in the experiments is much less than the dose used in hospital for tumour diagnosis. The ^{18}F decays by β^+ decay with the emission of a positron. Each positron rapidly annihilates with an electron, giving rise to a pair of 511 keV γ-rays which are emitted almost exactly back-to-back. The two γ-rays are simultaneously detected in the two detectors and define a trajectory passing close to the source. The location algorithm for tracking a single particle (Parker et al., 1993) has been developed from the principle that all the uncorrupted γ-ray trajectories for a given set of events should meet (to within the resolution of the camera) at a point in space where the tracer is located as shown in Fig. 1. The point can be found by minimising the sum of perpendicular distances to the various trajectories. Theoretically, all of the γ-rays emitted from a tracer should be back to back, and joint at the tracer position. However, in practice, many

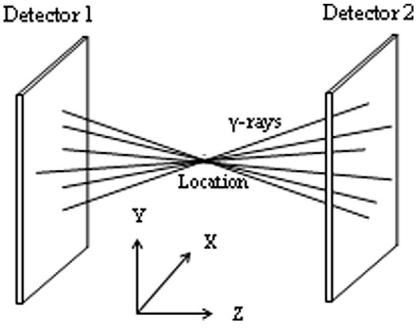

Fig. 1. Schematic diagram of PEPT for single particle.

γ-rays are corrupted and are not back to back. The location algorithm is used to discard the corrupt events, whose trajectories are broadcast randomly in space and do not in general pass close to the true particle location. The location is then recalculated using just the uncorrupted events. From successive locations, the velocity of the labelled particle can be found as it passes through the view of the camera (Parker, Allen, et al., 1997; Parker, Broadbent, Fowles, Hawkesworth, & McNeil, 1996; Parker, Dijkstra, Martin, & Seville, 1997; Parker, Forster, Fowles, & Takhar, 2002).

To track multiple particles, the tracers are labelled at different levels of radioactivity. For a given set of events, most γ-rays originate from the tracer with the strongest radioactivity. Thus, the most active tracer can be located by using the single particle tracking technique while the trajectories from the remaining tracers are regarded as corrupt trajectories. The first point which minimizes the sum of perpendicular distances to the various trajectories will be close to the strongest tracer. Those passing furthest away are discarded and the minimum distance point recalculated using the remaining subset. The iteration procedure continues until it is believed that all corrupt trajectories have been discarded and the location of the strongest tracer is calculated using just the uncorrupted events from the strongest tracer. Trajectories passing close to the located tracer are then removed from the dataset. The locations of the second and the third tracers are calculated in a similar way. The Multiple-PEPT technique is briefly described below.

For a selected set S of sequential trajectories $L_1,\ldots L_N$ which are recorded as data from the camera, the sum of distances from any point (x, y, z) to the γ-ray trajectories can be stated as follows.

$$D_s(x,y,z) = \sum_s \delta_i(x,y,z) \tag{1}$$

where $\delta_i(x, y, z)$ is the distance of the ith trajectory from the point (x, y, z).

To get the minimum sum of distances, the minimum solution must be obtained by

$$\begin{cases} \frac{\partial D_s(x,y,z)}{\partial x} = 0 \\ \frac{\partial D_s(x,y,z)}{\partial y} = 0 \\ \frac{\partial D_s(x,y,z)}{\partial z} = 0 \end{cases} \tag{2}$$

From Eq. (2), the minimum distance point (x_0, y_0, z_0) can be obtained as the first approximation. The mean deviation of these trajectories from the minimum distance point is then

$$d_s(x_0,y_0,z_0) = D_s(x_0,y_0,z_0)/N(S) \tag{3}$$

where $N(S)$ is the number of events in the set S.

The distance $\delta_i(x_0, y_0, z_0)$ of the ith trajectory from the point (x_0, y_0, z_0) is calculated for a given set of trajectories. The trajectories for which $\delta_i(x_0, y_0, z_0)$ is larger than $kd_s(x_0, y_0, z_0)$ are discarded, where k is a fixed parameter. This leaves a subset S_1 of events and a new (smaller) mean deviation $d_{s1}(x_1, y_1, z_1)$, from which an improved location (x_1, y_1, z_1) of the strongest tracer is calculated. The algorithm proceeds until only a specified fraction f of the initial trajectories remains, i.e. terminates at step n, where $N(S_n) = fN(S)$.

The parameter k determines the rate at which trajectories are discarded. Values of k between 1 and 1.5 have been investigated. The optimum lies somewhere between these two extremes (Parker et al., 1993).

If the parameters f_1, f_2 and f_3 are defined as the first-, second- and third-tracer fractions of the initial trajectories respectively and

another parameter ρ as the fraction of the desired trajectories in the entire original set S, the specified fraction f of the initial trajectories is equal to ρf_1 for the first strongest tracer. The parameter ρ has been investigated, and its optimum value lies between 0.20 and 0.33 (Parker et al., 1993).

After the strongest tracer is located, trajectories passing close to the located tracer are then removed from the dataset. In a similar way, repeating the above procedure, the locations of the second and the third tracers are then calculated.

And then the amount of γ-rays is recalculated around each located tracer for the entire original set S of trajectories to make sure the first, second and third highest amount of γ-rays around the tracers correspond to the first, second and third strongest tracers respectively.

The final outcome is that the subsets S_{F1}, S_{F2} and S_{F3} of trajectories are selected from the original set, from which the locations of tracers 1, 2 and 3 are calculated as their minimum distance points (x_{F1}, y_{F1}, z_{F1}), (x_{F2}, y_{F2}, z_{F2}) and (x_{F3}, y_{F3}, z_{F3}) respectively during the time interval covered by these subsets. Each event L_i has its time of measurement t_i recorded, and the location thus arrived at is considered to represent the tracers' position at time

$$t = \frac{1}{N_F}\sum_{S_F} t_i \tag{4}$$

where $N_F \equiv N(S_F)$ is the number of trajectories in the final subset, and $S_F = S_{F1} \cup S_{F2} \cup S_{F3}$.

Having located the tracers once, the new set starts immediately after trajectories have been discarded in the previous set.

2.2. Reconstruction of translational and rotational motions

Translational and rotational motions of any regular shape solid can be reconstructed by tracking three tracer particles if the positions of the particle are well designed. This paper uses cubed potato as an example to demonstrate the reconstructions. The best way to reconstruct the solid translational and rotational motions easily in a three-dimensional space is

(i) to place two tracers at the ends (a + b) of any side
(ii) and the third at any opposite corner (c),

so that the line ac goes through the centre of mass m as shown in Fig. 2A. This is shown in Fig. 2A. (Yang et al., 2008b). The reconstruction consists of three steps: (i) reconstruction of the centre of the solid using the three tracked locations on the solid to obtain solids translational motion, (ii) reconstruction of the three tracked locations on the solid by using the known size of the cubed solid to improve the accuracy of the three tracked locations, and (iii) reconstruction of solids rotational motion using the three improved locations and the centre of cubed solid. Details of the reconstruction of solids rotational and translation motions can be found in Yang et al. (2008b).

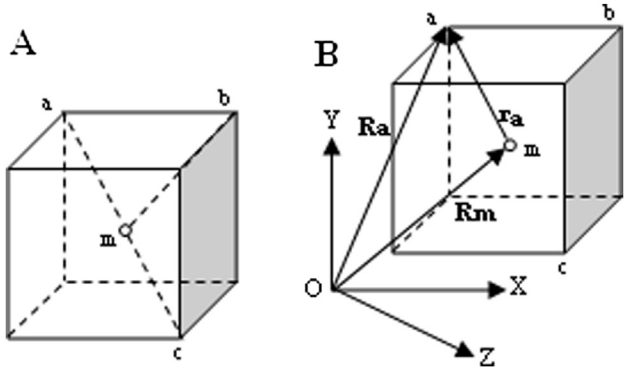

Fig. 2. Geometry of the labelled solid in three-dimensional space (A: the reconstruction of the centre of the cube, B: coordinate scheme for the solid rotation of a rigid body).

2.3. Reconstruction of the centre of cubed potato

If the length of a side of the cube is S, the following equations can be obtained from Fig. 2A.

$$|\overrightarrow{am}| = \left|\overrightarrow{bm}\right| = |\overrightarrow{cm}| = \frac{\sqrt{3}}{2}S \tag{5}$$

Thus the function

$$\left(\left|\overrightarrow{bm}\right| - \frac{\sqrt{3}}{2}S\right)^2 + \left(|\overrightarrow{am}| - \frac{\sqrt{3}}{2}S\right)^2 + \left(|\overrightarrow{cm}| - \frac{\sqrt{3}}{2}S\right)^2 \tag{6}$$

will equal zero if the distances are correctly found by the algorithm. Therefore, a function of $\vec{m}$ is defined,

$$y = f(\vec{m}) \equiv \left(\left|\overrightarrow{bm}\right| - \frac{\sqrt{3}}{2}S\right)^2 + \left(|\overrightarrow{am}| - \frac{\sqrt{3}}{2}S\right)^2 + \left(|\overrightarrow{cm}| - \frac{\sqrt{3}}{2}S\right)^2 \tag{7}$$

so by minimization of the $f(\vec{m})$, the centre of the cube can be identified. By tracking the three tracer positions at the corners a, b and c respectively, the motion of the centre of the cube m can be found. This represents the solid translational motion.

2.4. Reconstruction of solid rotational motion in a three-dimensional space

From Fig. 2B, the velocity of "a" relative to "m" (Smith & Smith, 2000, pp. 254–269) is

$$\dot{\mathbf{r}}_a = \mathbf{u}_a \times \mathbf{r}_a \tag{8}$$

where $\mathbf{u}_a$ is angular velocity, and $\mathbf{u}_a = (\omega_x, \omega_y, \omega_z)$.

The actual velocity of "a" will therefore be

$$\dot{\mathbf{R}}_a = \dot{\mathbf{R}}_m + \mathbf{u}_a \times \mathbf{r}_a \tag{9}$$

Thus

$$\mathbf{V}_a = \mathbf{V}_m + \mathbf{u}_a \times (\vec{a} - \vec{m}) \tag{10}$$

In a similar way,

$$\mathbf{V}_b = \mathbf{V}_m + \mathbf{u}_b \times \left(\vec{b} - \vec{m}\right) \tag{11}$$

$$\mathbf{V}_c = V_m + \mathbf{u}_c \times (\vec{c} - \vec{m}) \tag{12}$$

where the velocity is calculated by three successive locations as follows.

$$V_x(t_i) = \frac{1}{2}\left(\frac{x(t_{i+1}) - x(t_i)}{t_{i+1} - t_i} + \frac{x(t_i) - x(t_{i-1})}{t_i - t_{i-1}}\right) \tag{13}$$

In a similar way, the velocity in y and z directions can be obtained.

For a rigid body, the angular velocity of any point in the rigid body round the mass-centre should be same, and described by $\boldsymbol{\omega}$.

If a function of $\boldsymbol{\omega}$ is defined as

$$\begin{aligned} y =& f(\boldsymbol{\omega}) \equiv |\mathbf{V}_a - \mathbf{V}_m - \boldsymbol{\omega} \times (\vec{a} - \vec{m})|^2 \\ &+ \left|\mathbf{V}_b - \mathbf{V}_m - \boldsymbol{\omega} \times \left(\vec{b} - \vec{m}\right)\right|^2 \\ &+ |\mathbf{V}_c - \mathbf{V}_m - \boldsymbol{\omega} \times (\vec{c} - \vec{m})|^2 \end{aligned} \tag{14}$$

the $\boldsymbol{\omega}$ can be calculated by the minimization of (14).

Then the observed internal spin rate of the cube can be calculated as in Eq. (15).

$$N = \frac{|\boldsymbol{\omega}|}{2\pi} \tag{15}$$

To find how the cube spin varies with their position, the can was divided by several 2 mm × 2 mm × 119 mm cuboids, the solid spin was calculated by using the average for the cube which the centre of the cube was captured by the cuboid, as described in (Yang et al., 2008b). Thus, the average cube spin rate $\overline{N}$ was given by

$$\overline{N}_j = \frac{1}{l}\sum_{i=1}^{l} N(j,i) \tag{16}$$

where $N(j, i)$ denoted the instantaneous spin rate for the ith position of the cube in the jth cuboid.

The statistic internal spin rate of the cube, (i) average of internal spin rate (μ) and (ii) the standard deviation of internal spin rate (σ), were obtained by the following equations:

$$\mu = \frac{1}{k}\sum_{j=1}^{k} \overline{N}_j \tag{17}$$

$$\sigma = \sqrt{\frac{\sum_{j=1}^{k} \left(\overline{N}_j - \mu\right)^2}{k}} \tag{18}$$

2.5. Cans and liquids

The experiments similar to those in Yang et al. (2008a), tracking 3 tracers in three liquids, were performed. The cans throughout this study were supplied by Stratford Foods Ltd, Stratford UK and measured 119 mm high with a diameter of 100 mm. The experiments were designed for the observation of the effect of solids fraction and liquid viscosity on solids rotational and translational motions. The liquids used were water, dilute golden syrup and golden syrup with viscosities of 0.001, 2 and 27 Pa s, respectively. For each liquid, the experiments were carried out at four solids fractions, which were 10, 20, 40 and 50% (v/v). The dilute golden syrup was a solution of the golden syrup in 23% water. The solids used were cubed potatoes with a dimension of approximate 12 mm. The density of potato was 1080 kg/m^3, the density of the dilute golden syrup 1319 kg/m^3, and the density of the golden syrup 1423 kg/m^3. In each run, the headspace used was 10% (v/v). The cans were rotated on a horizontal tube roller at 12 rpm anticlockwise, as shown in Fig. 3. The three tracers had iso-density with respect to the cubed potato, were initially labelled with radioactivity: 3.1 MBq, 15.5 MBq and 8.8 MBq. To reconstruct the rotation of the cubed potato and the centre of the cube easily, two tracers were placed at the corners (labelled a and b in Fig. 2A) of any side and the third tracer at any opposite corner of the cubed potato (labelled c in Fig. 2A). All experiments were performed at the ambient temperature.

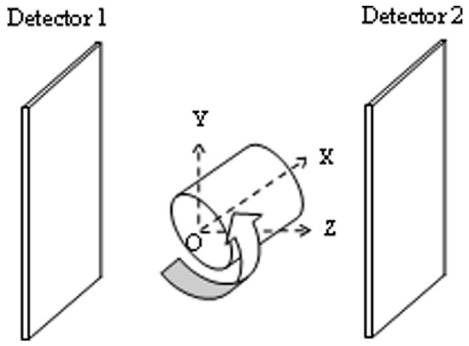

Fig. 3. Geometry of the rotating can in three-dimensional space.

3. Results and discussion

3.1. Effect of liquid viscosity and solids fraction on solids translational speed

Since the results are very similar for the solids fractions of 40% and 50%, this paper only gives the details for the solids fractions of 10%, 20% and 40%. Fig. 4 shows the speed of can body. Figs. 5–7 present translational speed of solids in the can over a 20-min period from the side view of YOZ plane.

In Fig. 4, the speed of can body was given by Eq. (19) at a given radius.

$$u(r) = 2\pi N r \tag{19}$$

where u is a speed of can body, and N is rotational speed of the can (revolutions per second).

In Figs. 5–7, solids speed was calculated by combining the velocities in y and z directions, as formulated in Eq. (20), because the velocity in the x direction is too small and negligible, compared to these in the y and z directions.

$$V = \sqrt{V_y^2 + V_z^2} \tag{20}$$

where V_y and V_z are solids velocities in y and z directions respectively.

From Figs. 5–7, it can be seen that the translational speed of solids in the can is related to the flow pattern of the bulk solids, and depends greatly on the liquid viscosity, the solids fraction, and the density difference between the solids and liquid as described in Yang et al. (2008b). The white space in the figures means that the tracer potato never reached the space. It is either head space in the can or the solids deposit on the can wall.

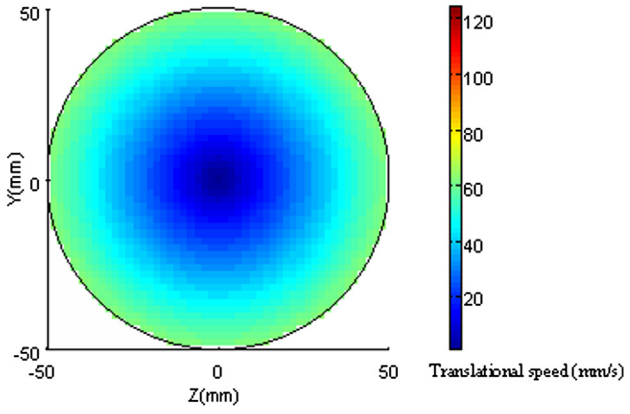

Fig. 4. Translational speed of the can examined as a solid body.

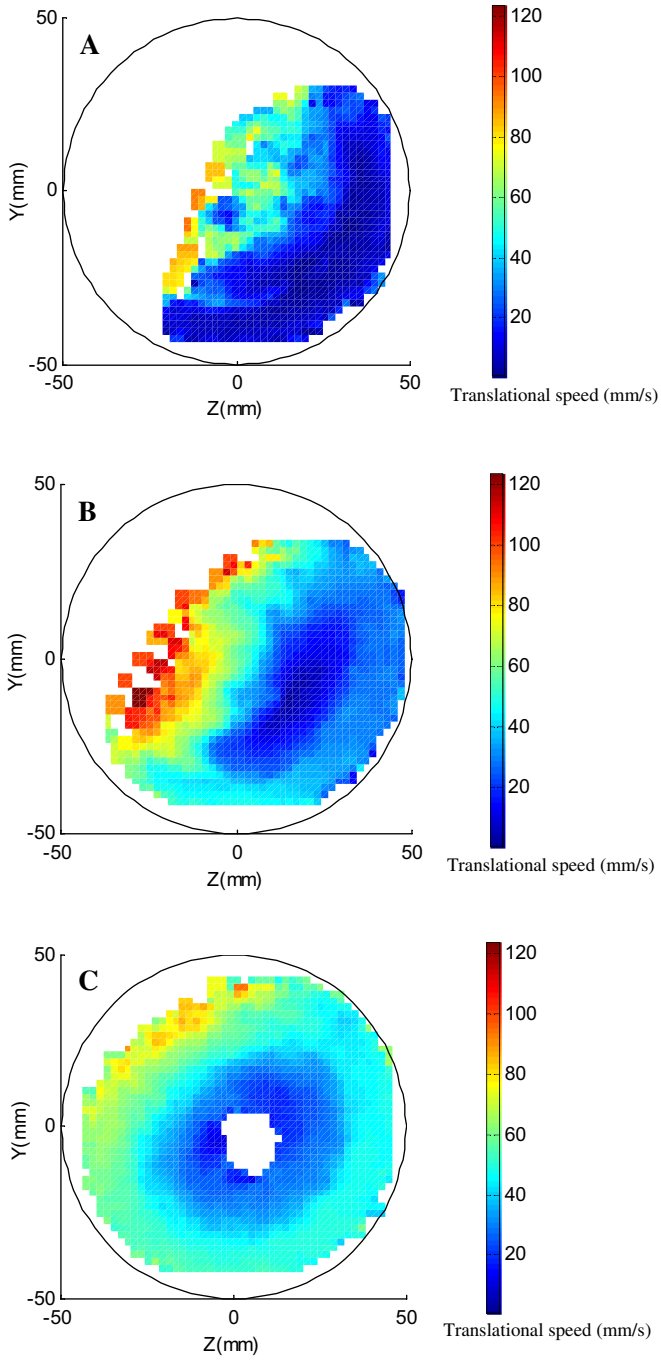

Fig. 5. Translational speed of solids in water (A: 10% solids, B: 20% solids, C: 40% solids).

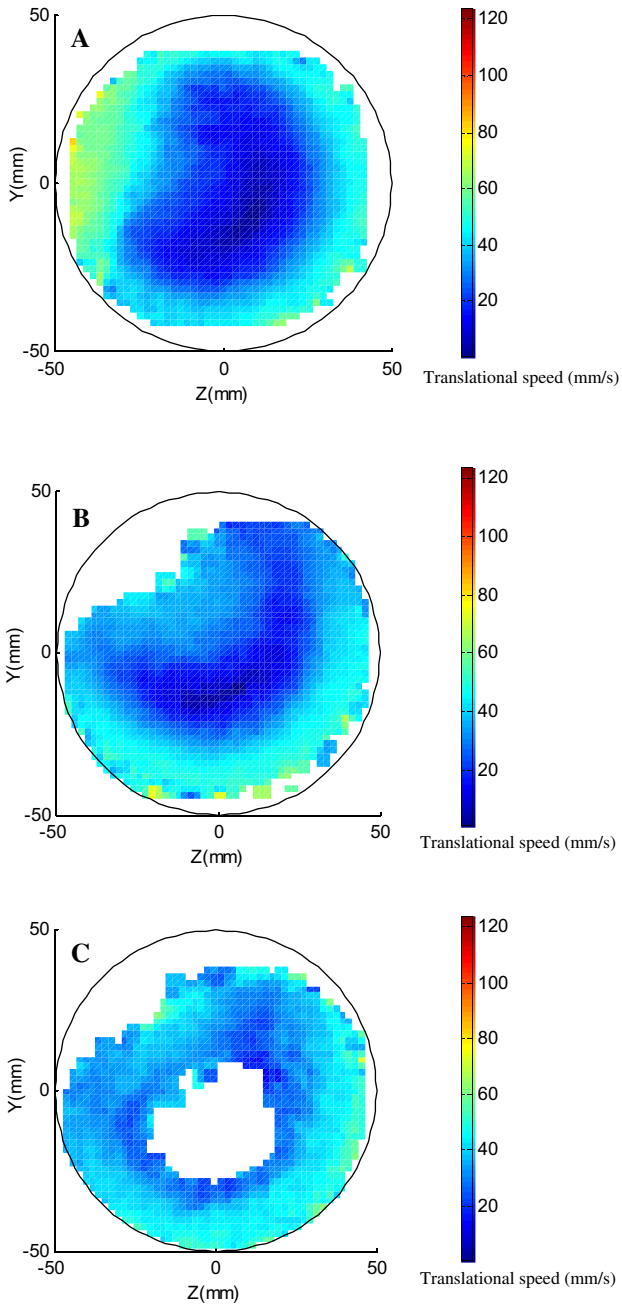

Fig. 6. Translational speed of solids in the golden syrup (A: 10% solids, B: 20% solids, C: 40% solids).

In water, solids in the can can be divided into two layers, namely, a 'passive' layer where solids are carried up by the can wall, and an 'active' layer where solids cascade down, as described in Yang et al., (2008a, 2008b). The passive layer was located at the region adjacent to the right-side wall, where solids moved almost as a packed rigid body and followed the can's rotation with a slightly slow speed. When solids were lifted to the top of the dynamic repose angle, the gravitation of the solids became a dominant drag force by comparing the density of potato with water. The solids slumped downwards over the passive layer, forming an active layer, where solids moved faster than the rotating can. Solids speed in the active layer was also dependent on the solids fraction within the can. It varied from 40 mm/s to 120 mm/s when the solids fractions were 10% (w/w) and 20% (w/w). The variation of solids speed in the active layer might give a good contribution to the agitation of the solid–liquid mixture in the can, therefore enhancing convective heat transfer. However, when the solids fraction increased to 40% (w/w), the solids speed was very close to that of solid body (Figs. 4 and 5C). Solids nearly followed a concentric flow and moved, more or less, as a rigid body, and acted as scraper to the surface reducing the boundary layer at the inner wall and enhancing heat transfer in the low viscosity liquid.

When the water was replaced by the golden syrup, the solids suspended in the golden syrup or stayed by the can wall due to the increased density and viscosity of the liquid. Solids were dragged upwards by the rotating can, fell down when they reached the headspace, the solids speed was relatively uniform (Fig. 6) and very

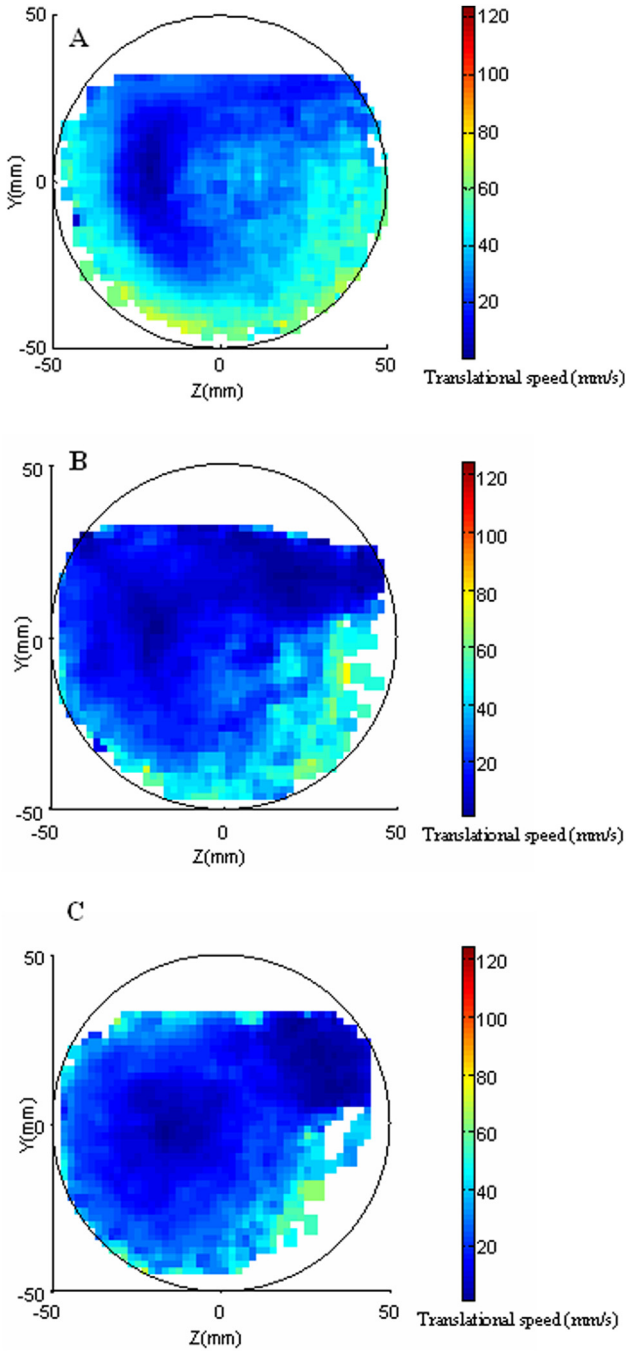

Fig. 7. Translational speed of solids in the diluted golden syrup (A: 10% solids, B: 20% solids, C: 40% solids).

similar to the speed of the can body (Fig. 4). It means that the solids for any fraction moved, more or less, as a nearly rigid body within the entire can, giving little contribution to the convective heat transfer from the wall to the centre.

In the diluted golden syrup, the solid flow pattern was different. The solids floated over the central region of the can. On the right side of the can, solids tended to move straight upwards, rather than (i) reposed on the wall of the can as observed in water or (ii) suspended in the golden syrup as observed in the undiluted golden syrup. On the left side of the can, solids tended to move close to the can wall. The upward speed was higher than the speed of solid body, particularly in the central region. The downward speed was less than the speed of solid body (Figs. 4 and 7). The speed distribution from the side view of YOZ plane was non-uniform. This non-uniform motion of the solids in the can will agitate the mixture and this might enhance the convective heat transfer. Through comparing the solids motion in the diluted and undiluted golden syrup, it can be seen that a slight dilution of the golden syrup might significantly change the solids motion, therefore the heat and mass transfer in the can.

3.2. Effect of liquid viscosity and solids fraction on solids spin

Figs. 8–10 present internal spin rate of solids over a 20-min period from the side view of YOZ plane. Fig. 11 shows the range of internal spin rate of solids over a 20 min period. Table 1 shows

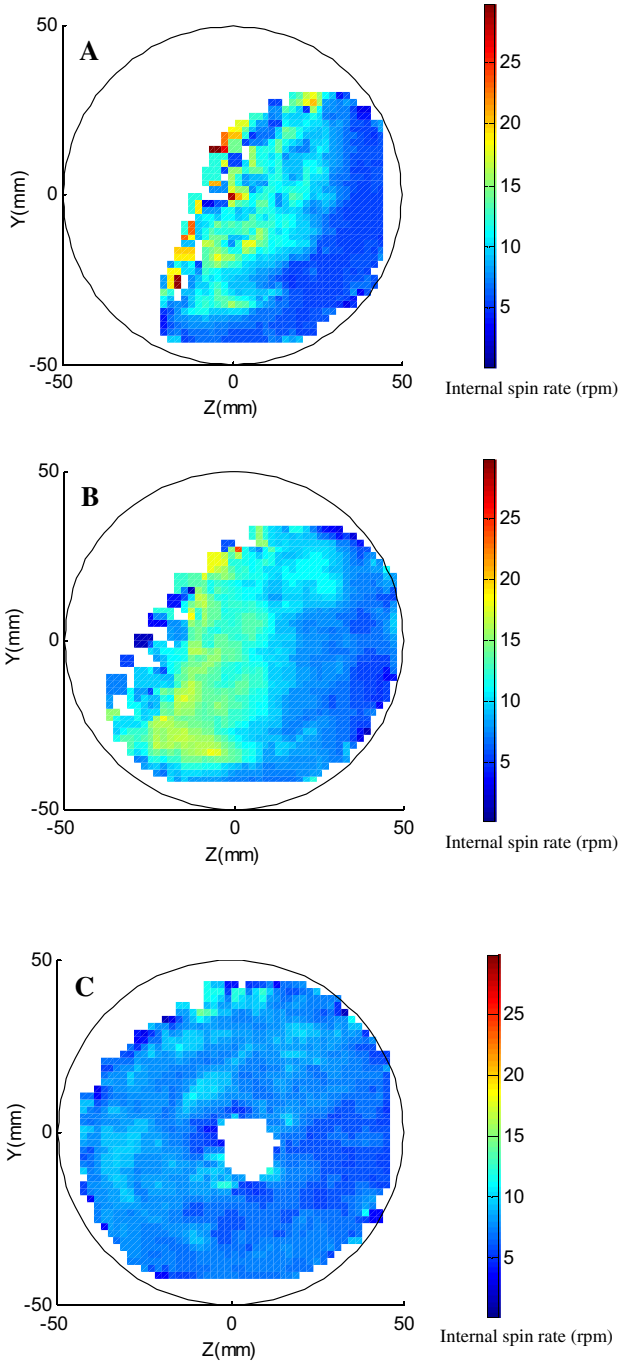

Fig. 8. Internal spin rate of solids in water (A: 10% solids, B: 20% solids, C: 40% solids).

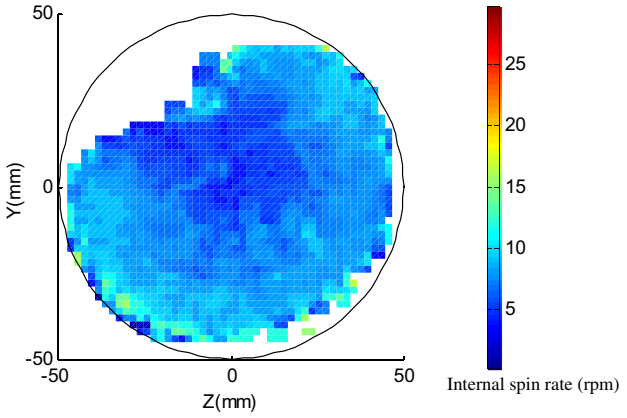

Fig. 9. Internal spin rate of solids in the golden syrup for the solids fraction of 20%.

internal spin rate of solids in the three liquids, calculated from Eqs. (17) and (18).

It is very interesting to note that the solids spin is related to the translational motion, and is dependent on the solids fraction, the liquid viscosity and the solids position within the rotating can.

3.2.1. Internal spin rate of solids in water

When the can was rotated in an anticlockwise direction, solids in water reposed on the right-side wall, and rotated upwards. The right-side wall applied a drag force to the solids near the can wall. The passive layer was located adjacent to the right-side wall, where solids moved almost as a packed rigid body. Within this layer, the solids spin was limited. The spin rate was therefore much more uniform and lower than that in the active layer as shown in Fig. 8. The active layer was at the left-side of the can, as shown in Fig. 5A and B. The collision and fast motion of solids resulted in the violent spin in the active regimes as shown in Fig. 8A and B. With increase in the solid fraction, the active regime was shrinking, and close to the headspace. The spin rate became much uniform within most of the can, except the region close to the headspace (Fig. 8C). The range of internal spin rate significantly decreased (Fig. 11A). It lay somewhere between (i) 3 and 30 rpm for the solids fraction of 10% (w/w), (ii) 1.8 and 24 rpm for the solids fraction of 20% (w/w), and (iii) 1.8 and 14.4 rpm for the solids fraction of 40% (w/w), and the average was 9.08, 9.94 and 7.36 rpm, respectively. The uniformity of the spin increased with the solids fraction (Table 1).

3.2.2. Internal spin rate in golden syrup

When the water was replaced by the golden syrup, the solids was suspended or stayed by the can wall due to the high liquid viscosity (27 Pa s) and liquid density (1422.5 kg/m^3). The solids moved more or less as a rigid body. The solids spin was slightly high in the region close to the can wall while it was slightly low at the central region of the can, as shown in Fig. 9. With increase in the solid fraction, a large stagnant core zone can be seen in the central region of the can (Fig. 6C), where the solid concentration was too high and limited the solids motion. The maximum internal spin rate almost kept a constant (Fig. 11B), the internal spin rate was between (i) 3 and 16.8 rpm for the solid fraction of 10% (w/w), (ii) 0.6 and 16.8 rpm for the solids fraction of 20% (w/w), and (iii) 1.2 and 17.4 rpm for the solids fraction of 40% (w/w), and the average was 8.12, 7.54 and 8.54 rpm, respectively. The solids spin was quite low. This further demonstrates that the rotation is determined by the flow pattern of the bulk solids, the solids concentration, the liquids viscosity, and the density difference between the solids and liquid.

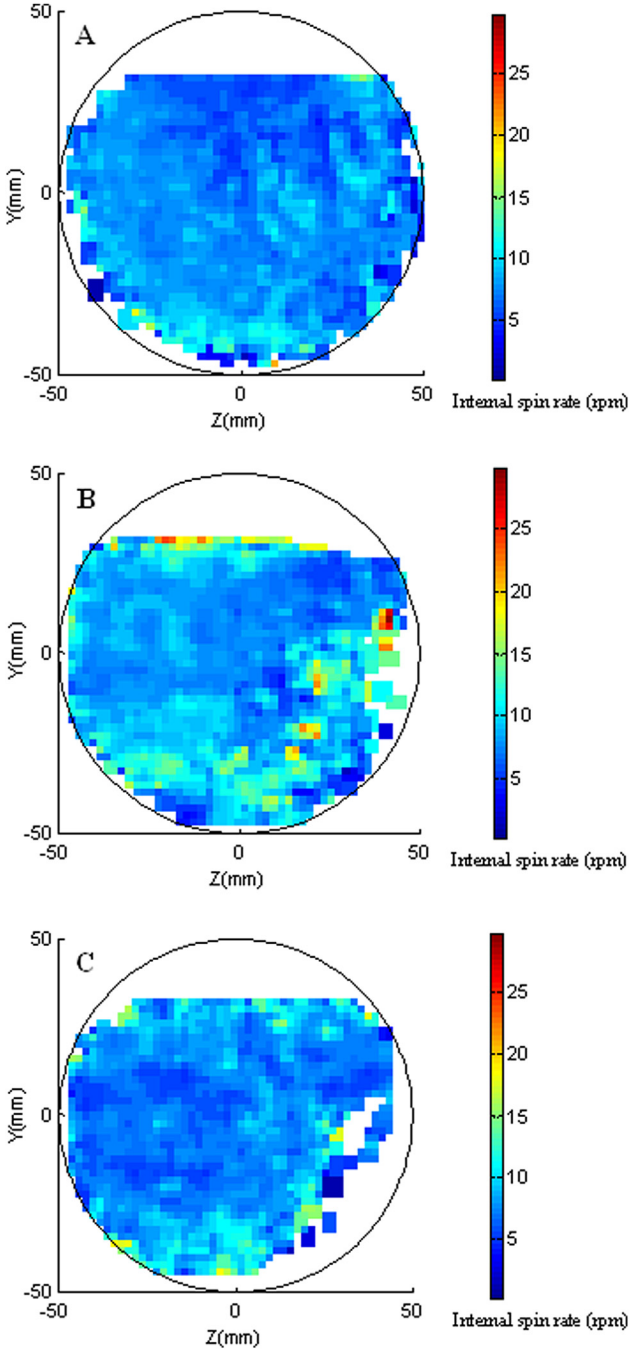

Fig. 10. Internal spin rate of solids in the diluted golden syrup (A: 10% solids, B: 20% solids, C: 40% solids).

3.2.3. Internal spin rate in the diluted golden syrup

When the solids were in the diluted golden syrup, the internal spin rate was changed significantly with the solids fraction. It was much higher at the solid fraction of 20% (w/w) than that at the solids fractions of 10% (w/w) and 40% (w/w). The solids spin was also much less uniform than that in water and in golden syrup as shown in Fig. 10. As well expected, in the diluted golden syrup, the buoyancy was dominated the solids motions, by comparing the densities between potato (1080 kg/m^3) and the dilute golden syrup (1318.6 kg/m^3). Solids floated in the can and tended to stay close to the headspace, leaving much more space in the region close to the right-side of the can. The solids tended to move straight upwards with a higher

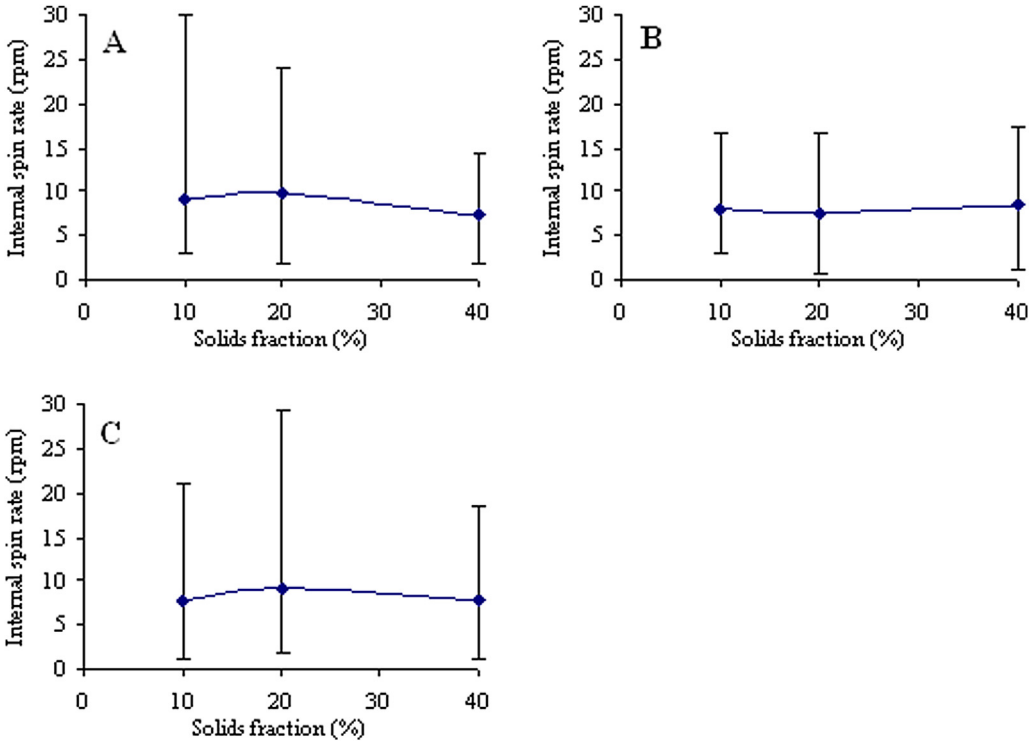

Fig. 11. The range of internal spin rate of solids over a 20 min period in the three liquids (A: water, B: golden syrup, C: diluted golden syrup).

speed, and no longer travelled as a rigid body following the can's rotation (Fig. 7). The space in the right-side of the can gave a high opportunity for solids collision, resulting in a much violent spin (Fig. 10). The internal spin rate was therefore higher in the region close to the head space due to the less limitation.

The internal spin rate of solids took a much wider distribution than that in golden syrup (Fig. 11B and C). The internal spin rate was between (i) 1.2 and 21 rpm, (ii) 1.8 and 29.4 rpm, and (iii) 1.2 and 18.6 rpm when the solid fractions were 10, 20 and 40% (w/w), respectively. The average value varied with the solids fraction. It was 7.69, 9.20 and 7.87 rpm for the solids fractions of 10, 20 and 40% (w/w) respectively. When the solid fraction increased from 10% to 20% (w/w), the average spin rate increased by 15%, and the uniformity of the spin decreased, as shown in Table 1. As described above, the solids no longer moved as rigid body as that in golden syrup, the internal spin rate increased by 19%, compared to the solids golden syrup at a solids fraction of 20% (w/w). This indicates that the solids spin in the diluted golden syrup might give a good convective heat transfer from the wall to the centre region of the can.

To demonstrate the solids spin, the three-dimensional cube at any time can be reconstructed by tracking multiple tracer particles. Part of the trajectories of solids spin in the three liquids is shown in Fig. 12, where the solids fraction was 20% (w/w). The cubes were pictured 7 times at regular intervals over a circulation period.

4. Conclusions

Solids translational and rotational motions within a food can be monitored simultaneously through non-invasively tracking three radioactively labelled tracers mounted at the corners of the solid.

The results indicate that translational motion and rotational motion are related to each other, both are dependent on the solids fraction, the liquid viscosity, and the solids location. In water (viscosity = 0.001 Pa s), solids spin was generally slow in the passive layer where particles were packed and reposed on the rising wall, but fast in the active layer where the space between solids is large. The uniformity of the spin rate within the entire can increased with the solids fraction as the distribution of

Table 1
Internal spin rate of solids in the three liquids.

Liquids	Solids fraction (%)	Max internal spin rate (rpm)	Min internal spin rate (rpm)	μ Average of internal spin rate (rpm)	σ Standard deviation of internal spin rate (rpm)
Water	10	30	3	9.08	3.86
	20	24	1.8	9.94	3.12
	40	14.4	1.8	7.36	1.31
Dilute golden syrup	10	21	1.2	7.69	1.81
	20	29.4	1.8	9.20	2.97
	40	18.6	1.2	7.87	2.15
Golden syrup	10	16.8	3	8.12	1.55
	20	16.8	0.6	7.54	2.03
	40	17.4	1.2	8.54	2.53

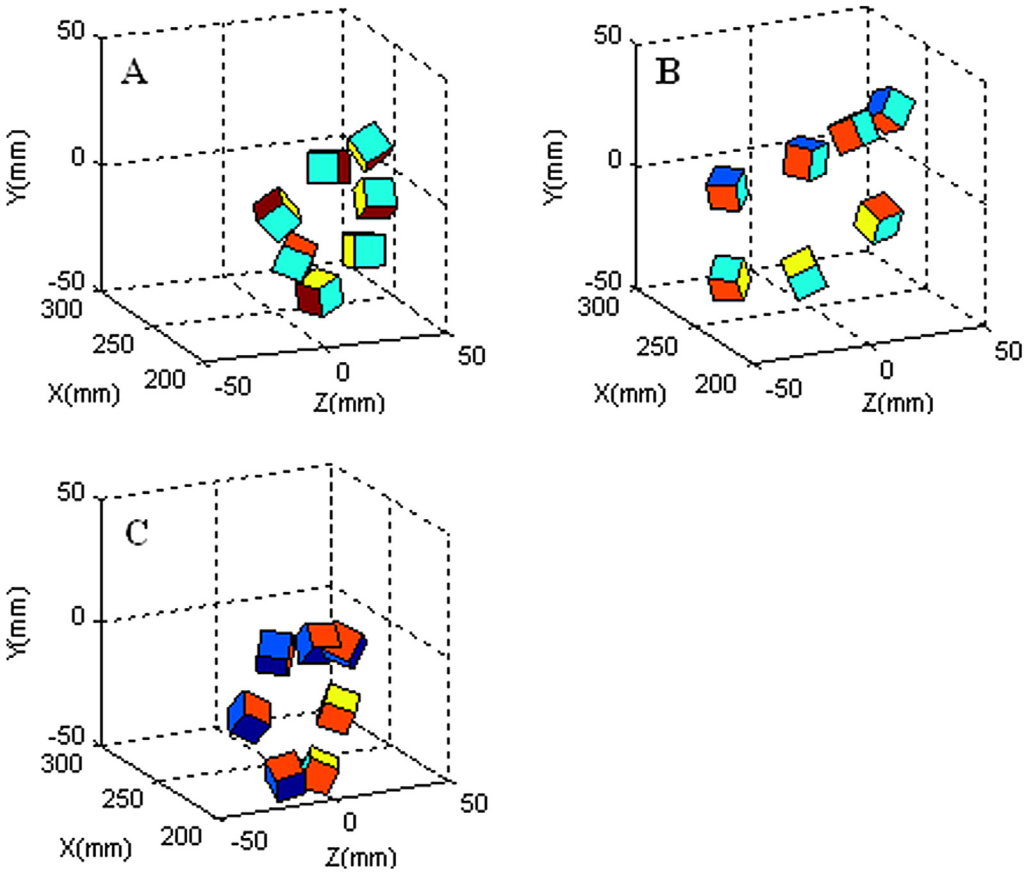

Fig. 12. Part of the trajectories of solids spin for the solids fraction of 20% (A: water, B: golden syrup, C: diluted golden syrup).

translational motion was closer to that of solid body. In the golden syrup (viscosity = 27 Pa s), the solids suspended in the golden syrup or stayed by the can wall. The internal spin rate and translational speeds were quite low, and slightly changed with the solids fraction. However, when the golden syrup was diluted by adding 23% of water (viscosity = 2 Pa s), the solids floated in the can. Due to the high buoyancy and low viscous drag force, solids tended to move straight upwards, rather than reposed on the wall of the can as observed in water or in the golden syrup. The internal spin and translational speeds were much higher and their distributions were much wider than that in golden syrup. Because of the violent and non-uniform distributed spin, the solids no longer travelled as a rigid body even though the solids fraction increased up to 40% (w/w). When a canned food is processed under these conditions, the solid motion might give a better convective heat transfer from the wall to the centre region of the can.

The results further demonstrated that Multiple-PEPT can be used to provide a deep insight into the heat mass transfer phenomena in food processing through the translational and rotational motion of solids.

Acknowledgements

The authors gratefully acknowledge financial support from the EPSRC and the Birmingham Positron Imaging Centre for this work.

References

Abdul Ghani, A. G., & Farid, M. M. (2006). Using the computational fluid dynamics to analyze the thermal sterilization of solid–liquid food mixture in cans. *Innovative Food Science & Emerging Technologies, 7*, 55–61.

Bakalis, S., Cox, P. W., Russell, A. J., Parker, D. J., & Fryer, P. J. (2006). Development and use of Positron Emitting Particle Tracking (PEPT) technique for velocity measurements in viscous fluids in pilot scale equipment. *Chemical Engineering Science, 61*, 1864–1877.

Barigou, M., Mankad, S., & Fryer, P. J. (1998). Heat transfer in two-phase solid–liquid food flows: a review. *Food and Bioproducts Processing, 76*, 3–29.

Chen, C. R., & Ramaswamy, H. S. (2002). Modeling and optimization of variable retort temperature (VRT) thermal processing using coupled neural networks and genetic algorithms. *Journal of Food Engineering, 53*, 209–220.

Cox, P. W., Bakalis, S., Ismail, H., Forster, R., Parker, D. J., & Fryer, P. J. (2003). Visualisation of three-dimensional flows in rotating cans using Positron Emission Particle Tracking (PEPT). *Journal of Food Engineering, 60*, 229–240.

Duursma, G. R., Glass, D. H., Rix, S. J. L., & Yorquez-Ramirez, M. I. (2001). PIV investigations of flow structures in the fluidised bed freeboard region. *Powder Technology, 120*, 2–11.

Fairhurst, P. G., Barigou, M., Fryer, P. J., Pain, J.-P., & Parker, D. J. (2001). Using positron emission particle tracking (PEPT) to study nearly neutrally buoyant particles in high solid fraction pipe flow. *International Journal of Multiphase Flow, 27*, 1881–1901.

Fan, X., Parker, D. J., & Smith, M. D. (2006a). Enhancing ^{18}F uptake in a single particle for positron emission particle tracking through modification of solid surface chemistry. *Nuclear Instruments and Methods A, 558*, 542–546.

Fan, X., Parker, D. J., & Smith, M. D. (2006b). Labelling a single particle for positron emission particle tracking using direct activation and ion-exchange techniques. *Nuclear Instruments and Methods A, 562*, 345–350.

García, M.-S. G., Balsa-Canto, E., Alonso, A. A., & Banga, J. R. (2006). Computing optimal operating policies for the food industry. *Journal of Food Engineering, 74*, 13–23.

Jun, S., & Sastry, S. (2007). Reusable pouch development for long term space missions: a 3D ohmic model for verification of sterilization efficacy. *Journal of Food Engineering, 80*, 1199–1205.

Kale, S. R., Ramezan, M., & Anderson, R. J. (1989). Measurement of particle rotational velocity using a laser anemometer. *Particle and Particle Systems Characterization, 6*, 59–63.

Kannan, A., & Sandaka, P. Ch. G. (2008). Heat transfer analysis of canned food sterilization in a still retort. *Journal of Food Engineering, 88*, 213–228.

Kızıltaş, S., Erdoğdu, F., & Palazoğlu, T. K. (2010). Simulation of heat transfer for solid–liquid food mixtures in cans and model validation under pasteurization conditions. *Journal of Food Engineering, 97*, 449–456.

Lareo, C., Branch, C. A., & Fryer, P. J. (1997). Particle velocity profiles for solid-liquid food flows in vertical pipes, Part I. Single particles. *Powder Technology, 93*, 23–34.

Lareo, C., Nedderman, R. M., & Fryer, P. J. (1997). Particle velocity profiles for solid-liquid food flows in vertical pipes, Part II. Multiple particles. *Powder Technology, 93*, 35–45.

Lee, H. Y., & Hsu, I. S. (1996). Particle spinning motion during saltating process. *Journal of Hydraulic Engineering, 122*, 587–590.

Legrand, A., Berthou, M., & Fillaudeau, L. (2007). Characterization of solid–liquid suspensions (real, large non-spherical particles in non-Newtonian carrier fluid) flowing in horizontal and vertical pipes. *Journal of Food Engineering, 78*, 345–355.

Mankad, S., Branch, C. A., & Fryer, P. J. (1995). The effect of particle slip on the sterilization of solid-liquid food mixtures. *Chemical Engineering Science, 50*, 1323–1336.

Mankad, S., & Fryer, P. J. (1997). A heterogeneous flow model for the effect of slip and flow velocities on food steriliser design. *Chemical Engineering Science, 52*, 1835–1843.

Mankad, S., Nixon, K. M., & Fryer, P. J. (1997). Measurements of particle-liquid heat transfer in system of varied solids fraction. *Journal of Food Engineering, 31*, 9–33.

Miri, T., Tsoukalis, A., Bakalis, S., Pistikopoulos, S., Rustem, B., & Fryer, P. J. (2008). Global optimisation of process conditions in batch sterilisation of food. *Journal of Food Engineering, 87*, 485–494.

Parker, D. J., Allen, D. A., Benton, D. M., Fowles, P., McNeil, P. A., Tan, M., et al. (1997). Developments in particle tracking using the Birmingham Positron Camera. *Nuclear Instruments and Methods A, 392*, 421–426.

Parker, D. J., Broadbent, C. J., Fowles, P., Hawkesworth, M. R., & McNeil, P. (1993). A positron emission particle tracking – a technique for studying flow within engineering equipment. *Nuclear Instruments and Methods A, 326*, 592–607.

Parker, D. J., Broadbent, C. J., Fowles, P., Hawkesworth, M. R., & McNeil, P. A. (1996). Positron emission tomography for process applications. *Measurement Science and Technology, 7*, 287–296.

Parker, D. J., Dijkstra, A. E., Martin, T. W., & Seville, J. P. K. (1997). Positron emission particle tracking studies of spherical particle motion in rotating drums. *Chemical Engineering Science, 52*, 2011–2022.

Parker, D. J., Forster, R. N., Fowles, P., & Takhar, P. N. (2002). Positron emission particle tracking using the new Birmingham positron camera. *Nuclear Instruments and Methods A, 477*, 540–545.

Reyes, J. N., Lafi, A. Y., & Saloner, D. (1998). The use of MRI to quantify multi-phase flow pattern transitions: an application to horizontal slug flow. *Nuclear Engineering and Design, 184*, 213–228.

Smith, P., & Smith, R. C. (2000). *Mechanics*. New York: John Wiley & Sons Ltd.

Tsuji, Y., Morkawa, Y., & Mizumo, O. (1985). Experimental measurement of the Magnus force on a rotating sphere at low Reynolds numbers. *Journal of Fluid Engineering, 107*, 484–488.

White, B. R. (1982). Two-phase measurements of saltating turbulent boundary layer flow. *International Journal of Multiphase Flow, 8*, 459–473.

White, B. R., & Schulz, J. C. (1977). Magnus effect in saltation. *Journal of Fluid Mechanics, 81*, 497–512.

Yang, Z., Fan, X., Bakalis, S., Parker, D. J., & Fryer, P. J. (2008a). Impact of solids fraction and fluid viscosity on solids flow in rotating cans. *Food Research International, 41*, 658–666.

Yang, Z., Fan, X., Bakalis, S., Parker, D. J., & Fryer, P. J. (2008b). A method for characterising solids translational and rotational motions using Multiple-Position Emission Particle Tracking (Multiple-PEPT). *International Journal of Multiphase Flow, 34*, 1152–1160.

Yang, Z., Parker, D. J., Fryer, P. J., Bakalis, S., & Fan, X. (2006). Multiple-particle tracking – an improvement for positron particle tracking. *Nuclear Instruments and Methods A, 564*, 332–338.